Actinic Wavelength Action Spectroscopy of the IO^- Reaction Intermediate

Benjamin I. McKinnon[a], Samuel J. P. Marlton[a], Boris Ucur[a], Evan J. Bieske[b], Berwyck L. J. Poad[c,d], Stephen J. Blanksby[c,d], Adam J. Trevitt[a]*

[a] *Molecular Horizons and School of Chemistry and Molecular Bioscience, University of Wollongong, Wollongong, New South Wales 2522, Australia*

[b] *School of Chemistry, The University of Melbourne, Victoria 3010, Australia*

[c] *Central Analytical Research Facility, Queensland University of Technology, Brisbane 4001, Australia*

[d] *School of Chemistry and Physics, Queensland University of Technology, Brisbane 4001, Australia*

E-mail: adamt@uow.edu.au
Phone: +61 2 4221 5545

Abstract

Iodinate anions are important in the chemistry of the atmosphere where they are implicated in ozone depletion and particle formation. The atmospheric chemistry of iodine is a complex overlay of neutral-neutral, ion-neutral and photochemical processes, where many of the reactions and intermediates remain poorly characterised. This study targets the visible spectroscopy and photostability of the gas-phase hypoiodite anion (IO^-), the initial product of the $I^- + O_3$ reaction, by mass spectrometry equipped with resonance-enhanced photodissociation and total ion-loss action spectroscopies. It is shown that IO^- undergoes photodissociation to $I^- + O$ (^3P) over 637 – 459 nm (15700 – 21800 cm^{-1}) due to excitation to the bound first singlet excited state. Electron photodetachment competes with photodissociation above the electron detachment threshold of IO^- at 521 nm (19200 cm^{-1}) with peaks corresponding to resonant autodetachment involving the singlet excited state and the ground state of neutral IO possibly mediated by a dipole-bound state.

Introduction

In the atmosphere, iodide (I^-) and its oxides, hypoiodite (IO^-) and iodite (IO_2^-) are relevant due to their reactivity towards ozone while iodate (IO_3^-) anions, alongside its conjugate acid (HNO_3) , have been implicated in particle formation[1-4]. Both I^- and IO_x^- (x =1, 2, 3) are detected in ground-based atmospheric gas measurements where IO_3^- concentrations exhibit a diurnal response, with lowest values detected during daytime, suggesting a link to photochemistry and night-time halogen chemistry[5]. In the lower stratosphere, both I^- and IO_3^- ions are present in detectable quantities and their fates in the presence of persistent ozone concentrations are under investigation[6]. The relevance of iodine oxoacids (both neutral and anions) as aerosol nucleation agents is apparent[4] but details on their photostability under actinic radiation is lacking.

In the gas phase, I^- reacts with O_3 in a stepwise process first producing IO^-, with subsequent reaction steps with O_3 to form $IO_2^- + O_2$ and ultimately $IO_3^- + O_2$ [7-10]. The overall rate limiting step in the formation of IO_3^- is the first step, $I^- + O_3$, while the subsequent steps involving IO^- and IO_2^- occur with high efficiency (91% and 84% of the collision rate, respectively). Interestingly, the slow reversible reactions of IO^- and IO_2^- (but not IO_3^-) with dioxygen have also been studied with the latter case regenerating IO^- [10]. Although the reaction kinetics and nucleation processes of these anion intermediates are becoming better characterised, there remains a lack of information on the photochemistry of these atmospheric anions, including the simplest iodine oxide anion, IO^-. The electron binding energies of the iodine oxides have been measured and suggest that IO^- (eBE = 2.3805 eV, 520 nm)[11-13] , IO_2^- (eBE = 2.575 eV, 481.5 nm)[12,14] but not IO_3^- (eBE = 4.70 eV, 263.8 nm)[14] may undergo photodetachment within the actinic window presenting a pathway to the corresponding neutral radicals. Recently, we demonstrated that photodissociation of the iodo-oxides anions, $IO_{1\text{-}2}^-$ occurs within the visible wavelength range (at 500 nm) and thus that these pathways are competitive with photodetachment at wavelengths relevant to the Earth's atmosphere. To explore this assertion, we present the first comprehensive investigation of the simplest iodine oxide, IO^-, using a combination of resonance enhanced photodissociation and ion-loss spectroscopy and

demonstrate that IO^- undergoes both photodissociation to $I^- + O(^3P)$ together with electron photodetachment to the neutral $IO^\bullet$ radical under visible wavelength irradiation.

Experimental Results

Visible light absorption by IO^- was investigated using tunable-laser irradiation of *m/z* selected IO^- ions confined within a room temperature linear quadrupole ion trap[15]. Action spectra were measured by monitoring both the generation of I^- photoproduct ions and the decrease in total ion count resulting from electron detachment. The thermodynamic limits for these pathways, and other plausible ones, are shown in Figure 1 with the four lowest-energy destruction pathways for IO^- ranked by their relative energy (as determined from NIST data) [16-19]. Assuming single-photon absorption, over the visible range, only $I^-(^1S) + O(^3P)$ photodissociation with an onset at 13729 cm^{-1} (728 nm) and $IO + e^-$ photodetachment with an onset at 19200 cm^{-1} (521 nm) are accessible. Notably the $I^-(^1S) + O(^3P)$ product pathway, the only photodissociation channel accessible in the visible wavelength range, generates $O(^3P)$, which can react with molecular oxygen to form ozone as per the Chapman ozone-oxygen cycle[20].

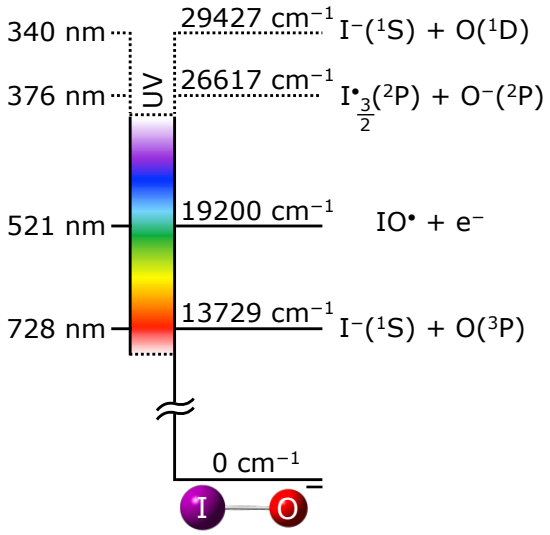

Figure 1: Schematic of the thermodynamic limits for the three lowest energy dissociation pathways of IO^- (from NIST data) [16-19]. The electron photodetachment energy is also included[13]. All energies are relative to the IO^- electronic ground state energy.

A representative single wavelength photodissociation mass spectrum of IO^- (*m/z* 143) obtained at 19231 cm^{-1} (520 nm) is shown in Figure S1. The sole product ion observed is *m/z* 127, assigned as I^- and assumed to form with $O(^3P)$. Photofragment O^- ions (*m/z* 16) are not expected given insufficient photon energy (*cf.* Figure 1) but such ions lie below the low *m/z* cut-off of the instrument and, consequently, we cannot rule out their formation from multiphoton processes. A plot of I^- photoproduct yield as a function of laser power at 520 nm (Figure S1 inset) displays a linear trend, consistent with a single photon photodissociation process.

The photodepletion spectrum of the IO^- signal (Figure 2A, obtained by plotting the difference in the total IO^- ion count with the laser on and the laser off) exhibits a structured band system spanning the 15700 – 22000 cm^{-1} range

(636.9 – 454.5 nm). The resonance-enhanced photodissociation (REPD) spectrum (Figure 2B) appears similar to the IO^- photodepletion spectrum but with better signal to noise and exhibits a broad structured band centred at 19000 cm^{-1} with an onset at 15700 cm^{-1}, which tails off to baseline at 21800 cm^{-1}. A series of peaks spaced by ~230 cm^{-1} is present within this broad band which, as will be shown, arise from a vibrational progression in an electronically excited state of IO^-. Peak locations are listed in Table S1. The presence of this extended vibrational progression implies that the anion excited-state is bound (at odds with some previous studies[21] but in accord with more recent reports[13]) and therefore suggests that the photodissociation of IO^- is mediated by electronic state curve crossing. It is notable that peaks expected to appear at 19410 and 20060 cm^{-1} appear to be supressed relative to neighbouring peaks and this will be discussed later.

The total ion-loss spectrum (Figure 2C), which presumably results from electron photodetachment from IO^-, is obtained by plotting the difference between the photodepletion and the photodissociation spectra, and is measured with an ion-trap storage time of 500 ms (allowing four laser pulses to irradiate the ion-packet per MS cycle). Since the I^- photoproduct is transparent in the visible region, the multi-shot experiment does not suffer additional complications arising from electron photodetachment from product ions. Over the spectrum, the total ion-loss signal rises sharply at photon energies greater than the EA of IO^- (2.3805 eV, 19198 cm^{-1})[13]. The discernible peaks in the ion-loss spectrum are attributed to resonant autodetachment and two of these peaks align with the supressed peaks in the REPD spectrum. At the higher energy end of the broad band, the signal does not return to zero (unlike the REPD spectrum) presumably due to electron photodetachment into the continuum. The weak signal between 18100-19200 cm^{-1} below the detachment threshold is likely due to absorption by hot ions. Overall, the S/N of Figure 2B is superior to Figures 2A and 2C as the detection of photoproduct ions is essentially a background free measurement.

The normalised ratio of photodissociation signal to the total ion-loss signal can be represented as a bias spectrum, which is shown in Figure 2D. At the photon energy corresponding to the EA, the two processes have equal yields, with photodissociation dominating below the EA. On the high energy side of the EA, electron loss dominates although the bias returns to zero in a few instances between the resonance peaks of the photodetachment. At photon energies greater than 20 000 cm^{-1} the photodepletion is dominated by electron loss.

The same analysis was performed with shorter (Figure S3) and longer (Figure S4) ion trap storage times, allowing for either 1 or 9 laser pulses, respectively, to irradiate the ions before they are scanned out of the ion trap. For the longer (9 pulse) case, the S/N of the total ion-loss spectrum is significantly improved with at least five peaks clearly apparent (labelled I—V). Under these conditions however, these spectra may be affected by saturation, this is particularly obvious for the REPD spectrum. The sharp features labelled I—V in Figure 2 generally align with peaks in the total ion-loss spectrum, and this will be discussed below.

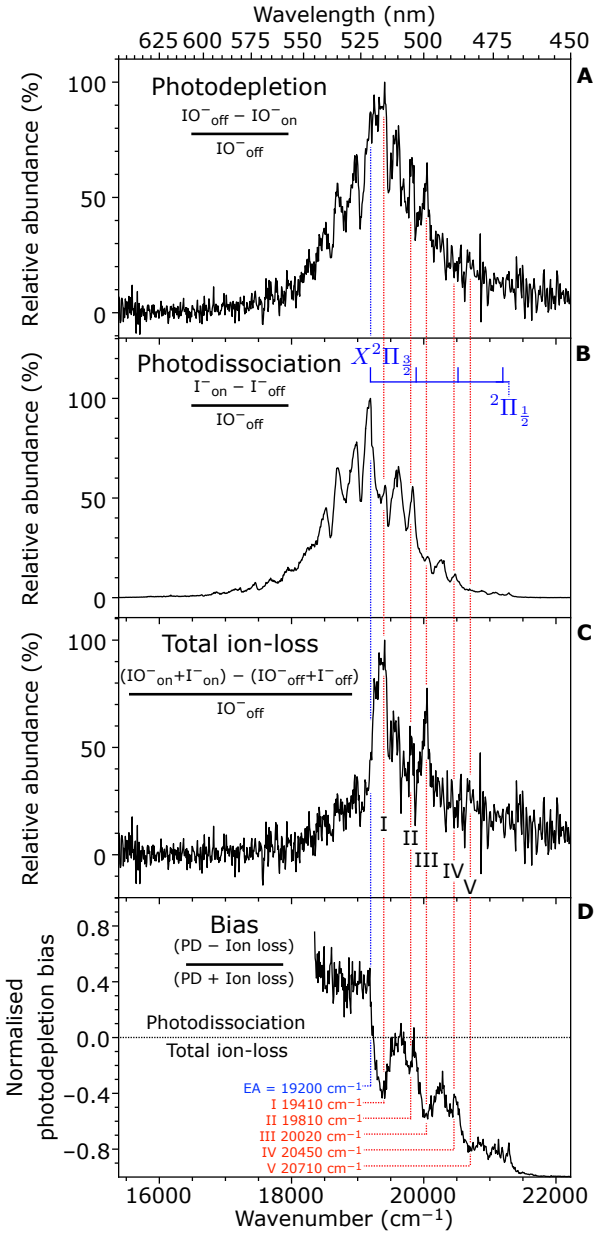

Figure 2: (A) The photodepletion spectrum of IO^- over the 15385 - 22222 cm^{-1} range (650 - 450 nm), (B) the resonance enhanced photodissociation REPD spectrum (I^- formation) and (C) total ion-loss spectrum. (D) is a bias plot where the difference of the photodissociation (PD) signal from (B) and the ion-loss signal from (C) is normalised to the combined signal. Spectra in (A), (B), (C) are all normalised to laser off signal (IO^-_{off}). These experiments correspond to IO^- ions stored in the ion-trap for 500 ms and subjected to four laser pulses per cycle. (Spectra corresponding to storage times of 220 ms (1 laser pulse) and 1000 ms (9 laser pulses) are included in the supporting information: Figures S3 and S4, respectively).

Computational Results

The calculated potential energy curves for the first seventeen electronic states of IO^- associated with the three lowest energy dissociation limits are plotted in Figure S5. Of these molecular states, five are within the energy range of the experiment (<22000 cm^{-1}) and were subjected to higher level (icMRCI+Q/aug-cc-pwCV5Z-PP)

treatment. These results are presented in Figure 3 with the calculated neutral ($^2\Pi_{3/2}$) potential energy curve also shown. The two spin-orbit states for the ground state of neutral IO are split by 2093(5) cm^{-1} such that the higher spin-orbit state ($^2\Pi_{1/2}$) resides at 21293 cm^{-1} relative to the IO$^-$ ground state (based on combining the experimental EA with computed spin-orbit values)[13], and thus this state is at the higher energy edge of the experimental range and is probably not relevant to the experiments discussed here.

The ground state of the anion ($X\,^1\Sigma^+$) is bound by *ca.* 26000 cm^{-1} and correlates to $I_{3/2}$ (^2P_u) + O$^-$ (^2P_u) fragments. The $1^1\Pi$ anion excited state is calculated to reside *ca.* 15000 cm^{-1} above the ground state and correlates to a $I_{3/2}$ (^2P_u) + O$^-$ (^2P_u) limit[22]. Crucially, this state is bound in the Franck-Condon (FC) region (17000 - 21500 cm^{-1}) and is the upper electronic excited state accessed in the visible wavelength excitation of IO$^-$. Another important feature is that the bottom of the $1^1\Pi$ anion well sits below the electron detachment threshold. Based on these calculations, intersystem crossing to the dissociative $1^3\Sigma^-$ state offers a pathway to I$^-$(^1S_g) + O(^3P_g), following photoexcitation to the $1^1\Pi$ state.

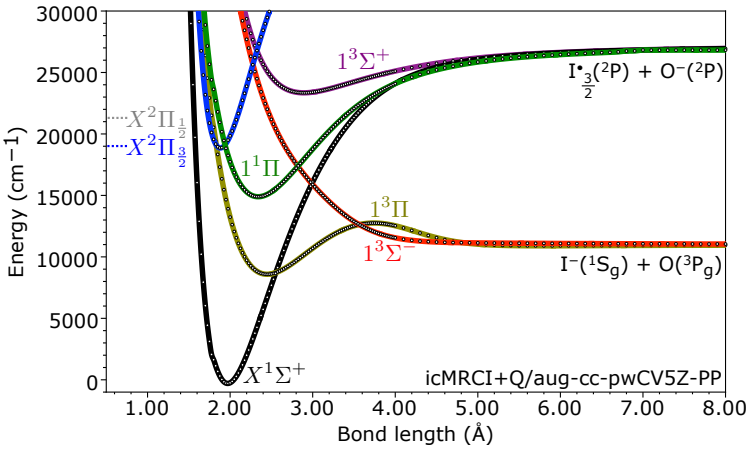

Figure 3: Potential energy curves for the five lowest in energy states of IO$^-$ and the $X\,^2\Pi_{3/2}$ state of IO calculated at the icMRCI+Q/aug-cc-pwCV5Z-PP level.

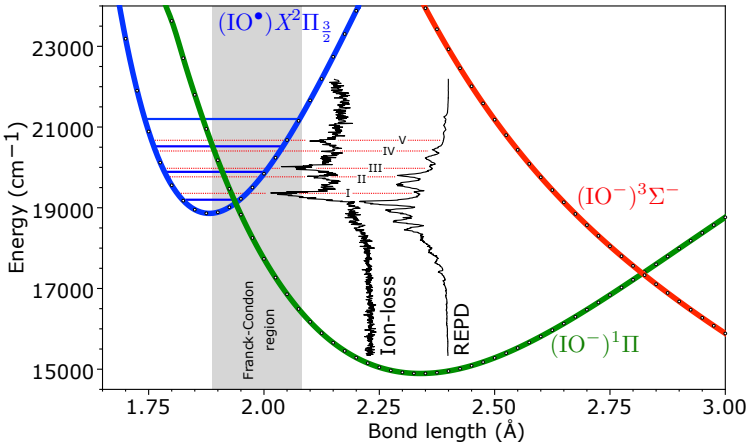

Figure 4: Relevant excited state potential energy curves from Figure 3 expanded over an internuclear distance range of 1.65 – 3.00 Å. The resonance enhanced photodissociation (REPD) from Figure S3 and the total ion-loss from Figure S4 are included for comparison.

Spectral analysis

Photodepletion and photodissociation

We now return to discuss the photodepletion and REPD spectra (Figure 2A and B) considering now the calculated potential energy curves and molecular parameters. Calculated molecular constants for the $1^1\Pi$ excited state of IO^- state are $T_e = 15040$ cm^{-1} with an equilibrium bond length $r_e = 2.34$ Å (see SI for more information). Using spline fits to the icMRCI single-point energies, the Duo program[23] provided vibrational constants: $\omega_e = 289.4$ cm^{-1} and $\omega_e\chi_e = 1.72$ cm^{-1}. The experimentally derived ground electronic state parameters for IO^-, reported by Gilles *et al.*, are $r_e = 1.929$ Å, $\omega_e = 581$ cm^{-1} and $\omega_e\chi_e = 4.37$ cm^{-1} [11,12]. The FC factors based on these parameters were calculated using the PGOPHER program[24] for the $1^1\Pi$ - $X\,^1\Sigma^+$ transition and the results are plotted in Figure S6A. To better match the simulated intensity profile with the experimental photodepletion spectrum the T_e value was raised from 15040 cm^{-1} to 16440 cm^{-1} (Figure S6B) and in this case the most intense transition corresponds to v' = 10. Alternatively, extending the excited state bond-length to 2.45 Å similarly shifts the FC simulation (Figure S6C). In this case, the most intense transition corresponds to v' = 16. In both cases the origin transition is predicted to be very weak, making it difficult to observe and assign. Ultimately, the correct vibrational numbering for the vibronic transitions requires an accurate value for T_e and because this calculation has an uncertainly on the order of ±1500 cm^{-1}, confident vibronic assignments are not possible. The simulation should be ultimately assessed against a direct absorption spectrum. An alternate strategy could be to probe these vibronic transitions with rare-gas tagging pre-dissociation spectroscopy. These spectra are also likely to be perturbed by mixing of states, as will be discuss in the next section, further complicating the analysis. Nevertheless, the similarities between the measured and simulated spectra suggest the calculations provide useful insights into the excited state probed in the experiments.

Total ion-loss spectrum

Contained within total ion-loss spectrum in Figure 2(C) are five peaks labelled I – V. The two strongest, I and III, are located at 19410 cm^{-1} and 20020 cm^{-1} and spaced by 610 cm^{-1}. The next peak, labelled V, is centred at 20710 cm^{-1} and spaced 690 cm^{-1} from III. The positions I, III, and V align with supressed peaks in the REPD spectrum (Figure 2B), as indicated with the vertical dotted lines. The two smaller peaks labelled II (19810 cm^{-1}) and IV (20450 cm^{-1}) are spaced by 640 cm^{-1}. These two peaks also align with peaks in the REPD spectrum but the corresponding REPD peaks look comparatively sharper as if the higher energy side of the peak is missing. The spacing of *ca.* 650 cm^{-1} in both sets is close to the known vibrational frequency for the ground state of the IO neutral: 682 cm^{-1}[13]. Figure 4 shows an expanded section of the key FC region from Figure 3 along with the REPD and total ion-loss spectra (from Figures S3 and S4) showing the position of peaks I–V and their relation to the known vibrational levels of the neutral IO electronic ground state. The neutral IO vibrational levels are located using known experimental values[13]. Peaks I-V do not align exactly with the vibrational energy levels of the $X\,^2\Pi_{3/2}$ IO neutral but there is a match with the vibrational energy level spacing that invites explanation.

Byfleet *et al*. report the dipole moment of IO as 2.45±0.05 D [25], which is very close to the critical value proposed for supporting a dipole bound state (DBS) [26-29]. Therefore, it is possible that the IO molecule supports DBSs associated with each of the IO neutral $X\,^2\Pi_{3/2}$ state vibrational levels and that the spectra are influenced by mixing

of the DBS and the anion $1^1\Pi$ valence state. Higher DBSs associated with IO $X\,^2\Pi_{3/2}$ excited vibrational states can decay through a vibrational autodetachment process. Within the diabatic formulism, the DBSs and valence $1^1\Pi$ IO^- states interact, leading to mixed vibronic states with both DBS and VS character. The situation is illustrated in Figure S7.

In this region of the spectrum, the vibrational energy level spacing for the $1^1\Pi$ state of IO^- is around a third that of neutral IO $X\,^2\Pi_{3/2}$ state. From Figure 4 it appears that vibrational levels associated with the $1^1\Pi$ state IO^- lie ≈100 cm^{-1} below and above the three lowest $X\,^2\Pi_{3/2}$ neutral vibrational levels. Neighbouring zero-order states associated with the $1^1\Pi$ state IO^- vibrational levels (shown in blue Figure S7) and the DBSs (shown in red Figure S7) presumably interact leading to mixed states having valence and DBS character. Relative rates for dissociation and electron detachment will depend on the respective rates for autodetachment and dissociation from the zero-order DBS and valence state and the mixing coefficients of each state. It is likely that transitions to the zero-order valence states are significantly stronger than those to the zero-order DBSs such that the intensity of the transition will depend on the coefficient for the valence state in the mixed state.

The fact that strong transitions give rise to detachment (peaks I and III) suggests that, when energetically allowed, the rate of electron detachment from the zero-order DBSs is more rapid than dissociation from the zero-order valence states. It is possible that the lower rotational levels of IO can support dipole bound states whereas the higher rotational levels cannot. This means that lower rotational states of some vibrational levels may detach whereas higher levels dissociate. There are hints that this happens in some of the asymmetric photodissociation peak shapes (*e.g.*, I and II).

A recent photoelectron study of IO^- using high-resolution velocity map imaging by Wang *et al.* [13] reported electron photodetachment (ePD) peaks at 19432 cm^{-1}, 20104 cm^{-1}, and 20721 cm^{-1}. These peaks align with peaks I, III, and V measured here. Peak I was attributed to the origin transition to the electronic excited $1^1\Pi$ state (230 cm^{-1} above the EA). Our experimental and computational results show that peak I is not the origin transition and that vibrational levels associated with the $1^1\Pi$ state reside below the EA. Also, Wang *et al.* located an ePD peak at 19829 cm^{-1} and surmised that it may be associated with an excited triplet anion state. This peak aligns with II and we conclude that it is a transition to a vibrational level associated with the $1^1\Pi$ state. Peak IV is not reported by Wang *et al.* An additional peak is reported by Wang *et al.* at 20951 cm^{-1} (labelled at VI in Figure S4, but not clearly resolved in our study) and is *ca*. 230 cm^{-1} from peak V and, like V, is likely a transition to an autodetaching level associated with the $1^1\Pi$ state of IO^-.

Conclusion

In summary, we report the visible spectroscopy and photostability of the IO^- reaction intermediate for the first time. Photodissociation of IO^- occurs over the 637 – 459 nm (15700 – 21800 cm^{-1}) range, producing I^- (^1S) + O (^3P). Transitions in this energy range access the first singlet excited state ($1^1\Pi$), likely followed by intersystem crossing to the $1^3\Sigma^-$ state leading to I^- (^1S) + O (^3P). Electron photodetachment occurs above the EA (19200 cm^{-1}) with peaks in the total ion-loss spectrum attributable to electron loss via autodetachment facilitated by mixing of

first singlet excited state ($1^1\Pi$) of IO^- and DBSs associated with vibrational levels of neutral IO in its ground electronic state ($X\,^2\Pi_{3/2}$).

These results provide further considerations for the formation and fate of IO^- in the atmosphere. That is, while electron photodetachment from IO^- (above the EA) feeds into accepted ($IO^\bullet$) radical-driven ozone depletion pathways[30], the observation of IO^- photofragmentation yielding I^- + O (^3P) represents a possible pathway for ozone regeneration *via* the Chapman cycle[20]. The wavelength dependence of these competing photochemistries may play a role in the reported diurnal behaviour of IO^- in the atmosphere[5]. Future investigation of the relative branching fraction between photo-detachment and -dissociation will be central to atmospheric models of iodo-oxide anions and flow-on implications for ozone concentrations and particle formation.

Methods

Experimental

Experiments were performed using a modified linear quadrupole ion trap mass spectrometer (Thermo Fisher Scientific LTQ XL) coupled with a tuneable, nanosecond pulsed, OPO laser (GWU-Lasertechnik flexiScan) pumped by a Spectra-Physics QuantaRay INDI, which is explained in detail elsewhere[31-33]. IO^- was created by first dissolving potassium iodate (KIO_3) in HPLC grade methanol (>99.7%) and subjected to electrospray ionisation to generate IO_2^- *via* source fragmentation. IO_2^- was then isolated in the ion-trap and dissociated via collision induced dissociation (CID) into IO^- that was isolated and interrogated *via* the laser in an MS^3 experiment.

Photodissociation experiments involved isolating and storing IO^- allowing irradiation with laser pulses, which was timed with a mechanical shutter synchronised with each individual isolation cycle. Photodissociation action spectra were recorded by a laser ON/OFF acquisition procedure. The ion signal with the laser off was subtracted from the ion signal with the laser on, to give the photoinduced signal, which was normalised by the total ion count when the laser is off. The accumulated raw data was processed *via* an in-house python script. Photodissociation action spectra were constructed by plotting the peak area of the only detected photoproduct, I^- (127 *m/z*), and normalised to the total ion count, against the photon energy. These experiments were performed using three different ion-trap isolation cycles: 220 ms, 500 ms, and 1000 ms which correspond to one, four, and nine laser shots, respectively. Different isolation times were used to increase the signal-to-noise ratios of the photodepletion spectra. Spectra with isolation periods of 500 ms are reported in the main text while spectra with isolation periods of 220 and 1000 ms are included in the supporting information.

Theoretical

Using the MOLPRO 2019.2 program[34] potential energy curves (PEC) were constructed by scanning the IO^- bond-length with the internally contracted multireference configuration interaction method with Davidson correction (icMRCI+Q) [35-38]. The state-averaged complete active space self-consistent field (CASSCF) method[39-42] was deployed to generate the wavefunction used in the icMRCI+Q calculation. CASSCF calculations were carried out for the seventeen states correlating with the three lowest energy dissociation limits[22], which are I^- (^1S_g) + O (^3P_g)

at 13729 cm^{-1}, I (^2P_u) + O^- (^2P_u) at 26617 cm^{-1}, and I^- (^1S_g) + O (^1D_g) at 29427 cm^{-1}. With this the seventeen states are labelled as follows: $1^3\Sigma^-$ and $1^3\Pi$ for the $I^-(^1S_g)$ + $O(^3P_g)$ channel, $X\,^1\Sigma^+$, $1^1\Sigma^+$, $1^1\Sigma^-$, $1^1\Pi$, $2^1\Pi$, $1^1\Delta$, $1^3\Sigma^+$, $2^3\Sigma^+$, $2^3\Sigma^-$, $2^3\Pi$, $3^3\Pi$, $1^3\Delta$ for the I(^2P_u) + O^-(^2P_u) limit, and $2^1\Sigma^+$, $3^1\Pi$, $2^1\Delta$ for the I^-(^1S_g) + O(^1D_g) limit[22]. The $X\,^1\Sigma^+$, $1^1\Pi$, $1^3\Sigma^-$, and $1^3\Pi$ states are necessary to understand our results and thus for these four states the icMRCI+Q method was deployed to yield accurate energies. The $X\,^2\Pi_{3/2}$ ground state of IO was also treated similarly. For both CASSCF and icMRCI+Q methods the oxygen atom was treated with the aug-cc-pwCV5Z basis set and for the iodine atom the pseudopotential approximation (-PP) extension was used[43-47]. The C_{2v} symmetry point group was used with the active space consisting of all 14 valence electrons distributed among the 8 valence molecular orbitals ($4a_1$, $2b_1$, $2b_2$). Spectroscopic constants of the $1^1\Pi$ state of IO^- were calculated using the Duo program[23] by fitting a spline to the icMRCI+Q PEC points with vibrational energies of the $1^1\Pi$ excited state determined using an RKR procedure. Experimental values from Gilles *et al.* were used for the $X\,^1\Sigma^+$ state[11,12].

References

1 Hoffmann, T., O'Dowd, C. D. & Seinfeld, J. H. Iodine oxide homogeneous nucleation: An explanation for coastal new particle production. *Geophysical Research Letters* **28**, 1949-1952 (2001).

2 Sakamoto, Y., Yabushita, A., Kawasaki, M. & Enami, S. Direct emission of I_2 molecule and IO radical from the heterogeneous reactions of gaseous ozone with aqueous potassium iodide solution. *The Journal of Physical Chemistry A* **113**, 7707-7713 (2009).

3 Moreno, C. & Baeza-Romero, M. T. A kinetic model for ozone uptake by solutions and aqueous particles containing I^- and Br^-, including seawater and sea-salt aerosol. *Physical Chemistry Chemical Physics* **21**, 19835-19856 (2019).

4 He, X.-C. *et al.* Role of iodine oxoacids in atmospheric aerosol nucleation. *Science* **371**, 589-595 (2021).

5 Frege, C. *et al.* Chemical characterization of atmospheric ions at the high altitude research station Jungfraujoch (Switzerland). *Atmospheric Chemistry and Physics* **17**, 2613-2629 (2017).

6 Koenig, T. K. *et al.* Quantitative detection of iodine in the stratosphere. *Proceedings of the National Academy of Sciences* **117**, 1860-1866 (2020).

7 Williams, S. *et al.* Negative ion chemistry of ozone in the gas phase. *The Journal of Physical Chemistry A* **106**, 997-1003 (2002).

8 Teiwes, R. *et al.* Atmospheric chemistry of iodine anions: elementary reactions of I^-, IO^-, and IO_2^- with ozone studied in the gas-phase at 300 K using an ion trap. *Physical Chemistry Chemical Physics* **20**, 28606-28615 (2018).

9 Teiwes, R., Elm, J., Bilde, M. & Pedersen, H. B. The reaction of hydrated iodide $I(H_2O)^-$ with ozone: a new route to IO_2^- products. *Physical Chemistry Chemical Physics* **21**, 17546-17554 (2019).

10 Bhujel, M. *et al.* Gas phase reactions of iodide and bromide anions with ozone: evidence for stepwise and reversible reactions. *Physical Chemistry Chemical Physics* **22**, 9982-9989 (2020).

11 Gilles, M. K., Polak, M. L. & Lineberger, W. Photoelectron spectroscopy of IO^-. *The Journal of chemical physics* **95**, 4723-4724 (1991).

12 Gilles, M. K., Polak, M. L. & Lineberger, W. Photoelectron spectroscopy of the halogen oxide anions FO^-, ClO^-, BrO^-, IO^-, $OClO^-$, and OIO^-. *The Journal of chemical physics* **96**, 8012-8020 (1992).

13 Wang, Y., Ning, C.-G., Liu, H.-T. & Wang, L.-S. High-Resolution Photoelectron Imaging and Photodetachment Spectroscopy of Cryogenically-Cooled IO^-. *The Journal of Physical Chemistry A* (2020).
14 Wen, H., Hou, G.-L., Huang, W., Govind, N. & Wang, X.-B. Photoelectron spectroscopy of higher bromine and iodine oxide anions: Electron affinities and electronic structures of $BrO_{2,3}$ and IO_{2-4} radicals. *The Journal of chemical physics* **135**, 184309 (2011).
15 Hansen, C. S., Kirk, B. B., Blanksby, S. J., O'Hair, R. A. & Trevitt, A. J. UV photodissociation action spectroscopy of haloanilinium ions in a linear quadrupole ion trap mass spectrometer. *Journal of The American Society for Mass Spectrometry* **24**, 932-940 (2013).
16 Gallagher, J. & Moore, C. E. *Tables of spectra of hydrogen, carbon, nitrogen, and oxygen atoms and ions*. (CRC press, 1993).
17 Peláez, R., Blondel, C., Delsart, C. & Drag, C. Pulsed photodetachment microscopy and the electron affinity of iodine. *Journal of Physics B: Atomic, Molecular and Optical Physics* **42**, 125001 (2009).
18 Neumark, D., Lykke, K., Andersen, T. & Lineberger, W. Laser photodetachment measurement of the electron affinity of atomic oxygen. *Physical Review A* **32**, 1890 (1985).
19 Dooley, K. S., Geidosch, J. N. & North, S. W. Ion imaging study of IO radical photodissociation: Accurate bond dissociation energy determination. *Chemical Physics Letters* **457**, 303-306 (2008).
20 Chapman, S. A theory of upperatmospheric ozone. *Mem. Roy. Meteor.* **3**, 103-125 (1930).
21 Minaev, B., Loboda, O., Vahtras, O., Ågren, H. & Bilan, E. Physical properties and spectra of IO, IO^- and HOI studied by ab initio methods. *Spectrochimica Acta Part A: Molecular and Biomolecular Spectroscopy* **58**, 1039-1053 (2002).
22 Herzberg, G. *Molecular spectra and molecular structure-Vol I. (Vol. 1.)*. (D. van Nostrand, 1945).
23 Yurchenko, S. N., Lodi, L., Tennyson, J. & Stolyarov, A. V. Duo: a general program for calculating spectra of diatomic molecules. *Computer Physics Communications* **202**, 262-275 (2016).
24 Western, C. M. PGOPHER: A program for simulating rotational, vibrational and electronic spectra. *Journal of Quantitative Spectroscopy and Radiative Transfer* **186**, 221-242 (2017).
25 Byfleet, C., Carrington, A. & Russell, D. Electric dipole moments of open-shell diatomic molecules. *Molecular Physics* **20**, 271-277 (1971).
26 Turner, J. Minimum dipole moment required to bind an electron—molecular theorists rediscover phenomenon mentioned in Fermi-Teller paper twenty years earlier. *American Journal of Physics* **45**, 758-766 (1977).
27 Jordan, K. D. & Wang, F. Theory of dipole-bound anions. *Annual review of physical chemistry* **54**, 367-396 (2003).
28 Simons, J. Molecular anions. *The Journal of Physical Chemistry A* **112**, 6401-6511 (2008).
29 Qian, C.-H., Zhu, G.-Z. & Wang, L.-S. Probing the critical dipole moment to support excited dipole-bound states in valence-bound anions. *The journal of physical chemistry letters* **10**, 6472-6477 (2019).
30 Alicke, B., Hebestreit, K., Stutz, J. & Platt, U. Iodine oxide in the marine boundary layer. *Nature* **397**, 572-573 (1999).

31 Ly, T. & Julian, R. R. Residue-specific radical-directed dissociation of whole proteins in the gas phase. *Journal of the American Chemical Society* **130**, 351-358 (2008).
32 Ly, T. *et al.* Reactions of simple and peptidic alpha-carboxylate radical anions with dioxygen in the gas phase. *Physical Chemistry Chemical Physics* **13**, 16314-16323 (2011).
33 Maccarone, A. T. *et al.* Direct observation of photodissociation products from phenylperoxyl radicals isolated in the gas phase. *J Am Chem Soc* **135**, 9010-9014 (2013).
34 Werner, H. J., Knowles, P. J., Knizia, G., Manby, F. R. & Schütz, M. Molpro: a general-purpose quantum chemistry program package. *Wiley Interdisciplinary Reviews: Computational Molecular Science* **2**, 242-253 (2012).
35 Knowles, P. J. & Werner, H.-J. An efficient method for the evaluation of coupling coefficients in configuration interaction calculations. *Chemical physics letters* **145**, 514-522 (1988).
36 Werner, H. J. & Knowles, P. J. An efficient internally contracted multiconfiguration–reference configuration interaction method. *The Journal of chemical physics* **89**, 5803-5814 (1988).
37 Knowles, P. J. & Werner, H.-J. Internally contracted multiconfiguration-reference configuration interaction calculations for excited states. *Theoretica chimica acta* **84**, 95-103 (1992).
38 Shamasundar, K., Knizia, G. & Werner, H.-J. A new internally contracted multi-reference configuration interaction method. *The Journal of chemical physics* **135**, 054101 (2011).
39 Knowles, P. J. & Werner, H.-J. An efficient second-order MC SCF method for long configuration expansions. *Chemical Physics Letters* **115**, 259-267 (1985).
40 Werner, H. J. & Knowles, P. J. A second order multiconfiguration SCF procedure with optimum convergence. *The Journal of chemical physics* **82**, 5053-5063 (1985).
41 Werner, H. J. & Meyer, W. A quadratically convergent multiconfiguration–self-consistent field method with simultaneous optimization of orbitals and CI coefficients. *The Journal of Chemical Physics* **73**, 2342-2356 (1980).
42 Werner, H. J. & Meyer, W. A quadratically convergent MCSCF method for the simultaneous optimization of several states. *The Journal of Chemical Physics* **74**, 5794-5801 (1981).
43 Peterson, K. A. & Dunning Jr, T. H. Accurate correlation consistent basis sets for molecular core–valence correlation effects: The second row atoms Al–Ar, and the first row atoms B–Ne revisited. *The Journal of chemical physics* **117**, 10548-10560 (2002).
44 Wilson, A. K., Woon, D. E., Peterson, K. A. & Dunning Jr, T. H. Gaussian basis sets for use in correlated molecular calculations. IX. The atoms gallium through krypton. *The Journal of chemical physics* **110**, 7667-7676 (1999).
45 Kendall, R. A., Dunning Jr, T. H. & Harrison, R. J. Electron affinities of the first-row atoms revisited. Systematic basis sets and wave functions. *The Journal of chemical physics* **96**, 6796-6806 (1992).
46 Woon, D. E. & Dunning Jr, T. H. Gaussian basis sets for use in correlated molecular calculations. V. Core-valence basis sets for boron through neon. *The Journal of chemical physics* **103**, 4572-4585 (1995).
47 Peterson, K. A., Shepler, B. C., Figgen, D. & Stoll, H. On the spectroscopic and thermochemical properties of ClO, BrO, IO, and their anions. *The Journal of Physical Chemistry A* **110**, 13877-13883 (2006).

Acknowledgements

A. J. T. and S. J. B. acknowledge financial support from the Australian Research Council (ARC) through the Discovery Project scheme (DP170101596). Computational resources provided by the Australian Government through the National Computation Infrastructure under an NCMAS grant. B. I. M, S. J. P.M. and B.U. are. Supported by Australian Government RTP Scholarships.

Author contributions

B.I.M. performed all experiments, data analysis and calculations. S.J.P.M. assisted with experimental and computational analysis. B.U. assisted with experiments. E.J.B and A. J. T contributed also to the analysis. A.J.T. directed and supervised the project, which was conceived by B.L.J.P, S. J. B, and A.J.T. All authors contributed to the authoring and editing of the manuscript.

Competing interests

Authors declare no competing interests